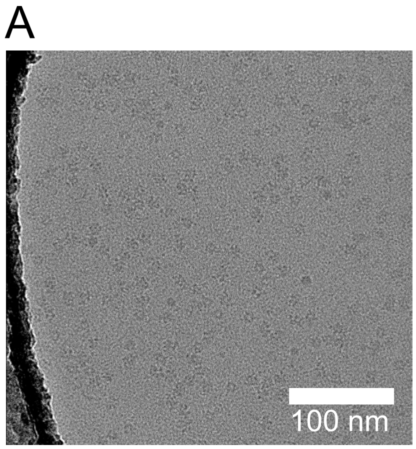

DnaBC micrograph

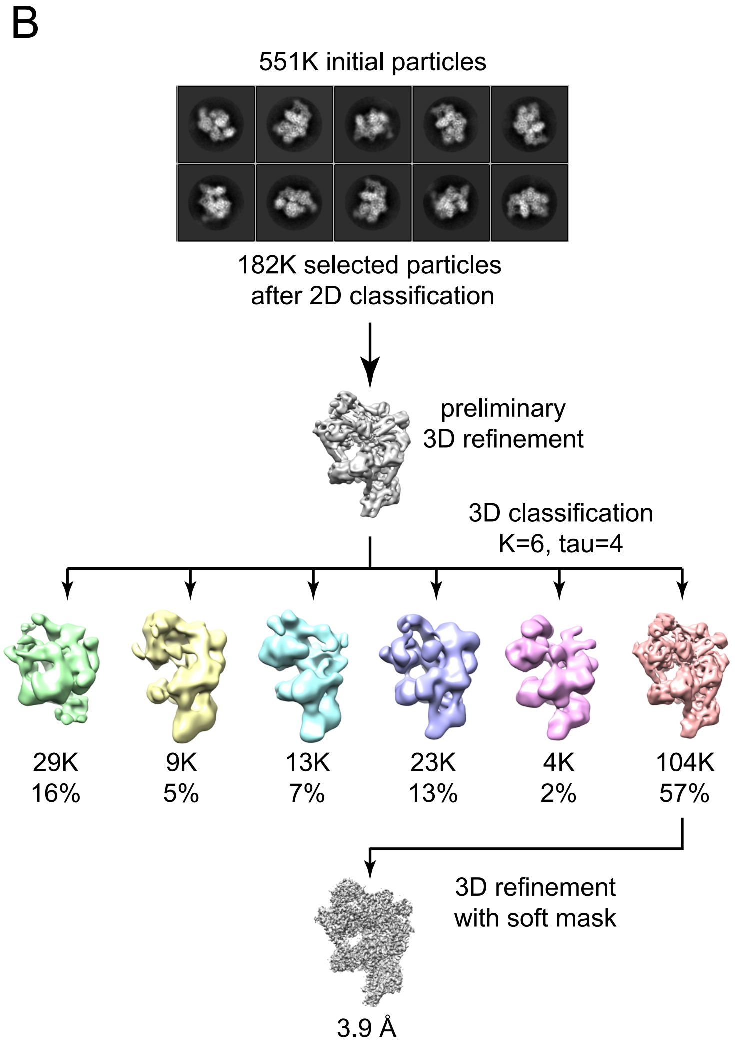

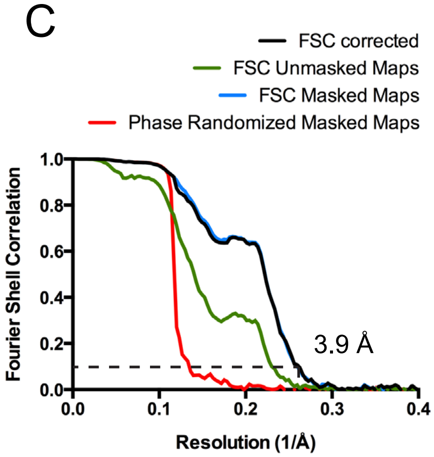

Fourier Shell Correlation

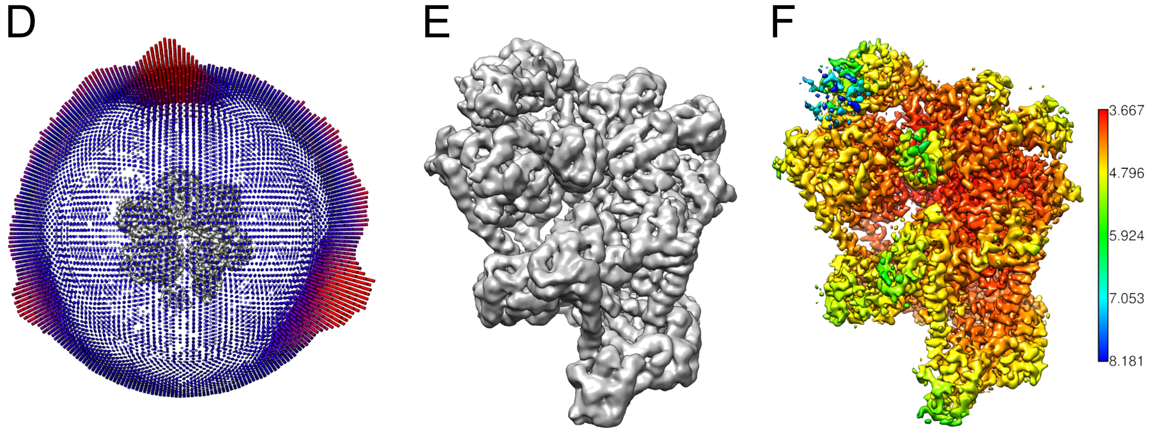

DnaBC
Angular distribution

DnaBC
unsharpened map

DnaBC
local resolution

Figure S1. Cryo-EM analysis and image processing of apo E. coli DnaBC, related to Figure 1.
(A) Cryo-EM micrograph of apo DnaBC complexes.
(B) Workflow of image processing of apo DnaBC particles.
(C) Fourier Shell Correlation of the final density map.
(D) Angular distribution plot showing the range of observed particle orientations.
(E) Unsharpened map of the DnaBC complex showing clear density for all protein domains.
(F) Local resolution of the final, sharpened map of the apo DnaBC complex.

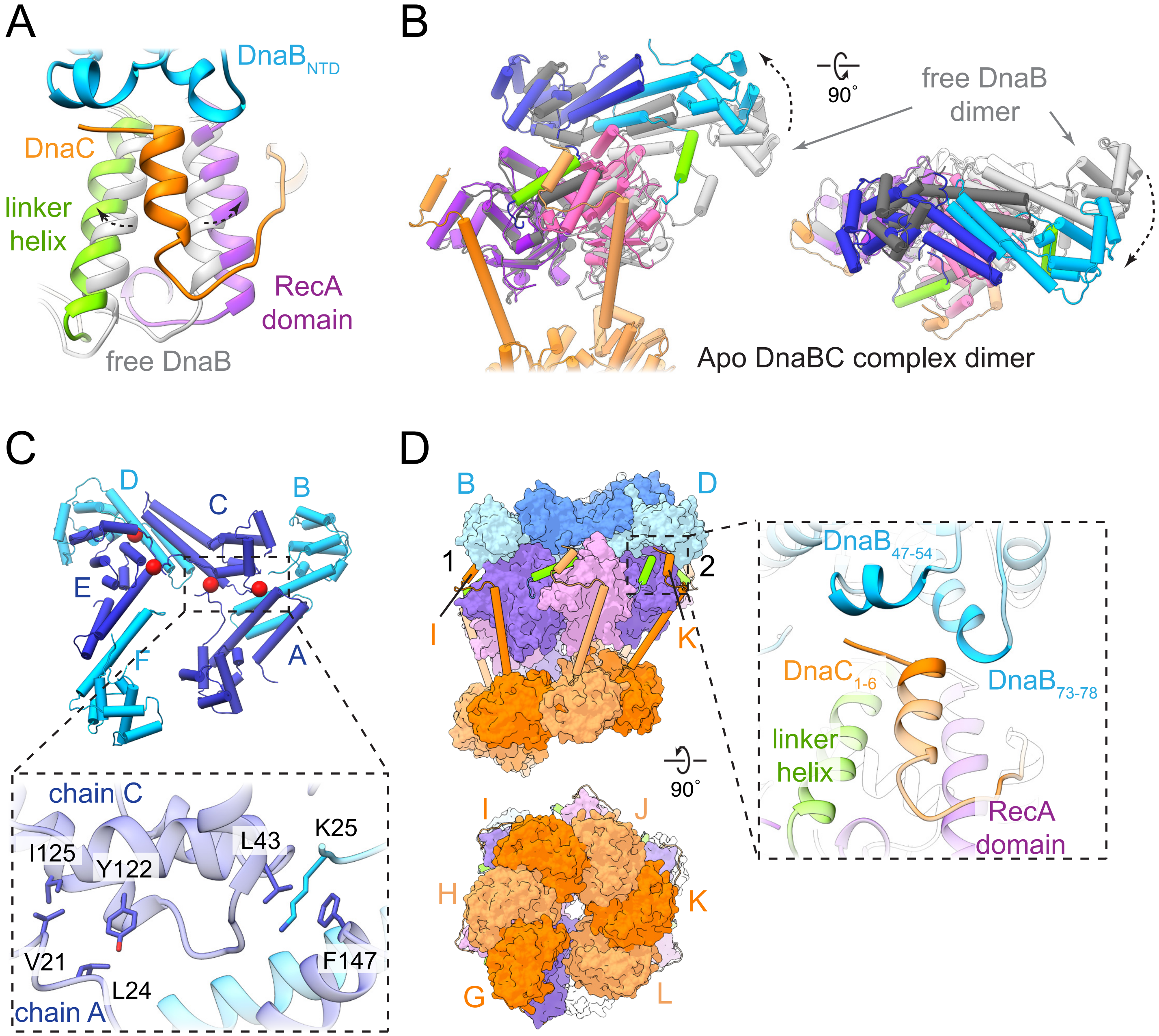

Figure S2. DnaBC interactions formed in the apo state, related to Figure 1.
(A) The interaction of the DnaC NTD wedges apart the interaction between the DnaB linker helix with a neighboring subunit of the helicase.
(B) DnaC binding remodels the disposition of the RecA domains and the N-terminal domain dimers of DnaB, leading to the formation of a constricted open state.
(C) Staircase-shaped, cracked/constricted arrangement of DnaB N-terminal domains. Red spheres mark the contact points between equivalent domains from different dimers (A-C and C-E). (Bottom) Detailed view showing some of the residues that mediate the interaction between equivalent regions of different DnaB NTD dimers.
(D) In two instances, the first α-helix of the DnaC NTD can be seen to interact with the globular head of the N-terminal domain. (Right) Close-up highlighting some of the areas involved in the interaction. The flexibility of the solvent exposed loops did not allow unambiguous modeling of the interacting side chains.

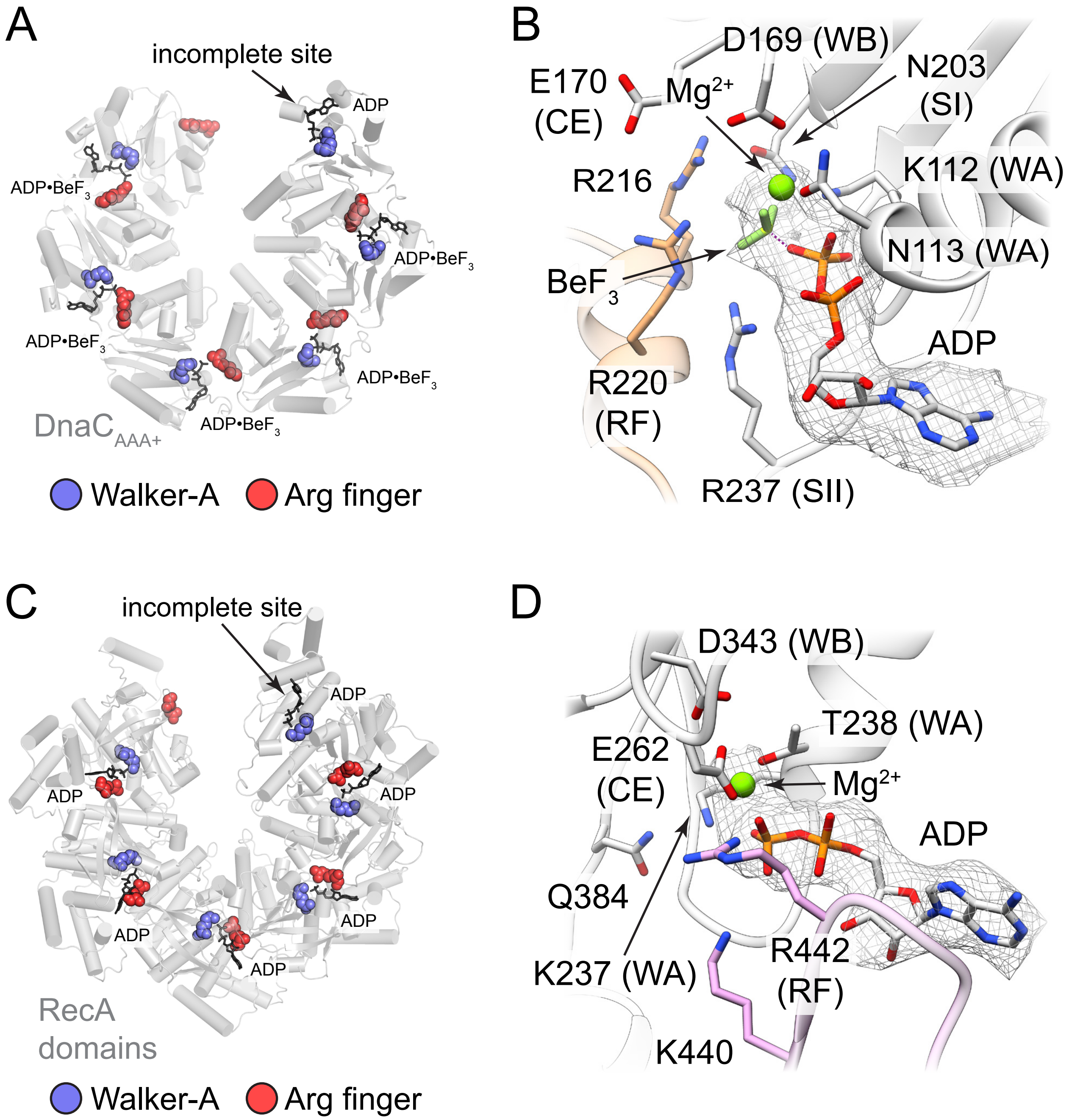

Figure S3. Helicase and loader active sites in the apo DnaBC complex, related to Figure 2.
(A) The DnaC active site is formed by catalytic residues located in two adjacent subunits. The crack in the ring leads to the formation of a single incomplete active site.
(B) Density showing that ADP•BeF3 is present in the nucleotide binding pocket of DnaC.
(C) The DnaB active site is formed by catalytic residues located in two adjacent subunits. The crack in the ring leads to the formation of a single incomplete active site.
(D) Density showing that only ADP is present in the nucleotide binding pocket of DnaB.

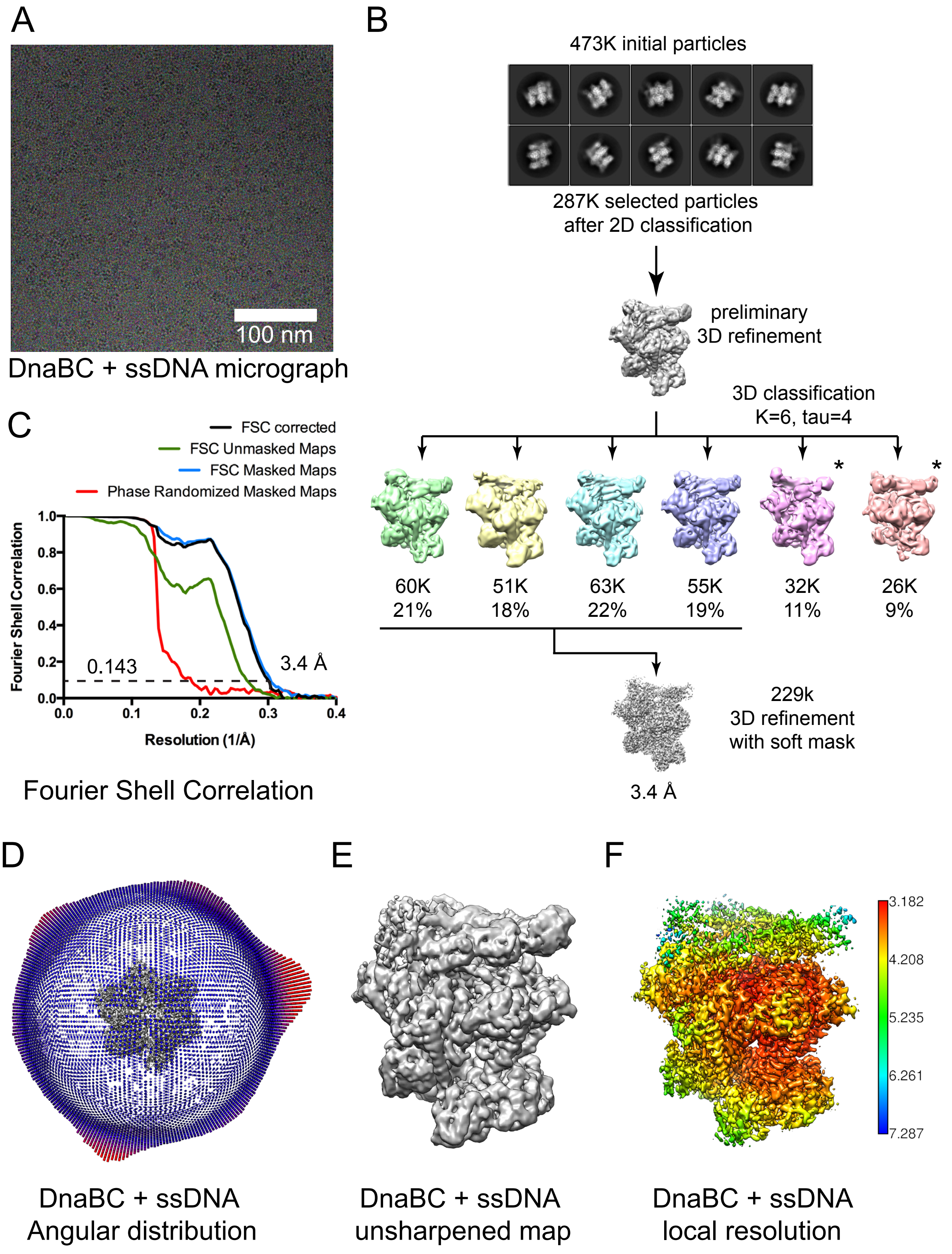

DnaBC + ssDNA micrograph

Fourier Shell Correlation

DnaBC + ssDNA Angular distribution

DnaBC + ssDNA unsharpened map

DnaBC + ssDNA local resolution

Figure S4. Cryo-EM and image processing of ssDNA-bound DnaBC, related to Figure 3.
(A) Cryo-EM micrograph of DnaBC complexes mixed with dT36.
(B) Workflow of image processing for ssDNA-bound DnaBC particles. The stoichiometry of the nucleic acid-bound complex is also 6:6, except in ~20% of the particles where one DnaC subunit appears to have dissociated (indicated by asterisks). The cryo-EM data did not reveal other stoichiometries, although we cannot rule out that other ratios might exist in different pre-helicase opening and post-loading states.
(C) Fourier Shell Correlation of the final density map.
(D) Angular distribution plot showing the range of orientations observed for ssDNA-bound DnaBC particles.
(E) Unsharpened map of the DNA-bound DnaBC complex showing density for all protein domains.
(F) Local resolution of the final, sharpened map. The main core of the complex shows resolution values that range between 3.2 and 3.8 Å. Some areas of the DnaB NTDs and of the subunits close to the crack are less ordered due to a reduced number of intermolecular contacts.

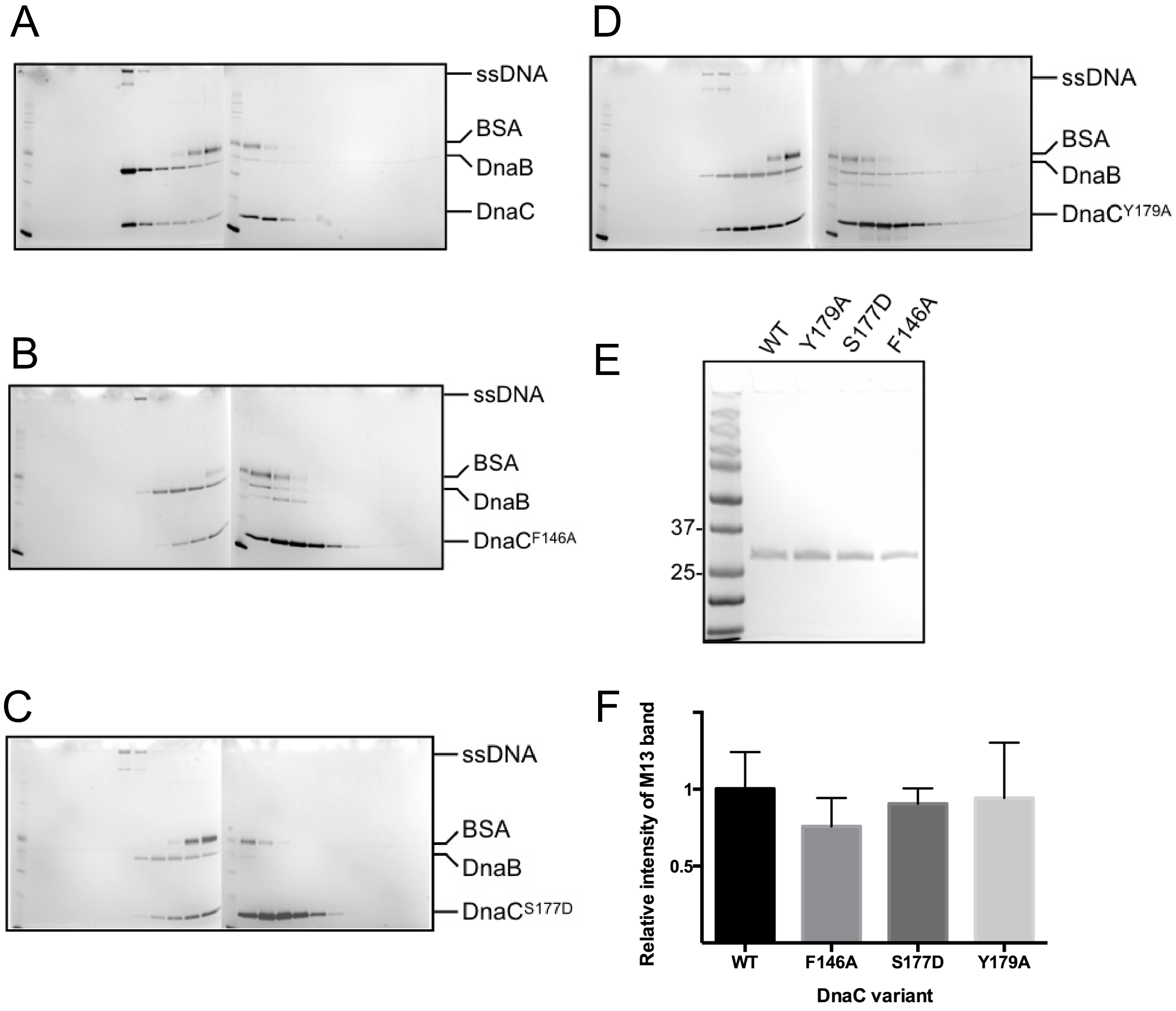

Figure S5. DnaB loading assays , related to Figure 5.
The role of DnaC residues seen to interact with ssDNA in loading DnaB was assessed using an M13-based assay (Fang et al., 1999). Representative gels are shown for (A) WT, (B) F146A, (C) S177D, and (D) Y179A. (E) Gel showing that comparable measured concentrations obtained for WT DnaC and DNA-binding deficient mutants indeed contain equimolar amounts of protein. (D) Relative intensity of the M13 band obtained in loading experiments with different DnaC variants. Data presented are from three independent experiments (mean ± SEM).

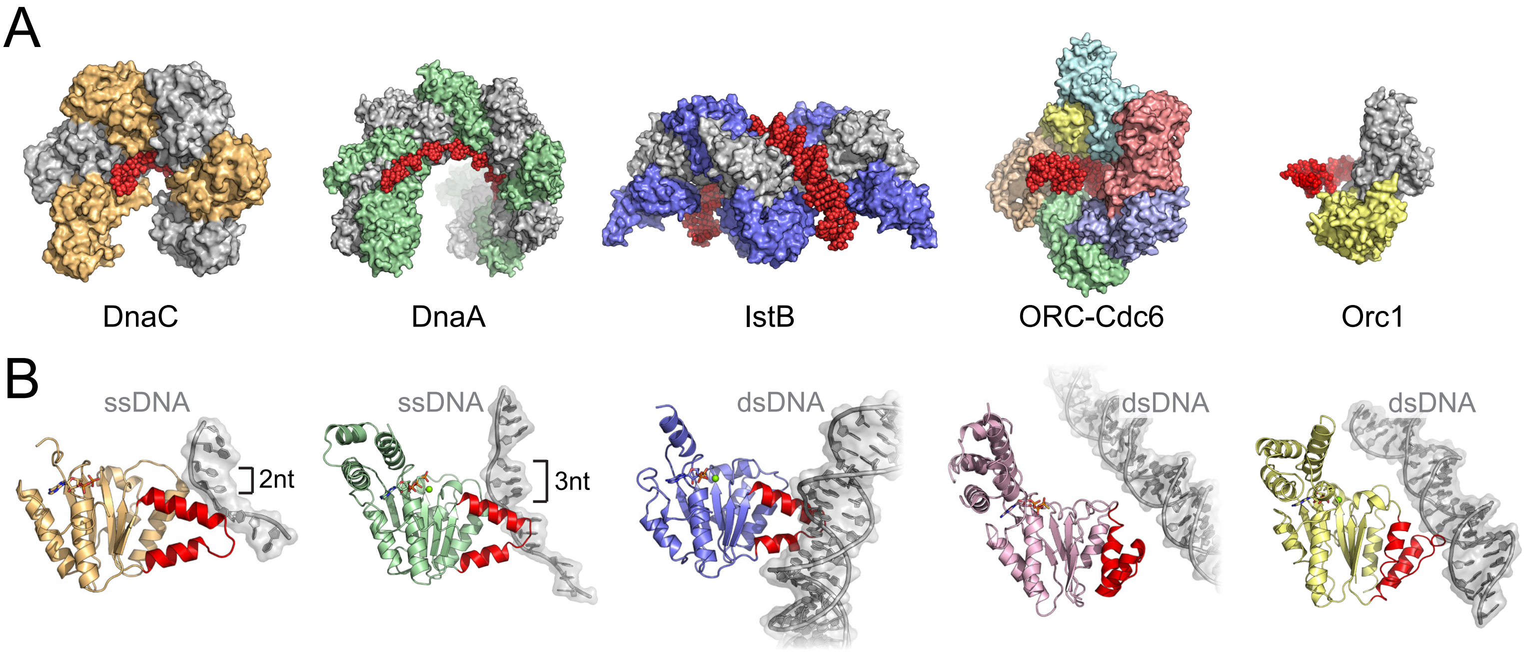

Figure S6. DNA binding strategies of initiator clade AAA+ proteins, related to Figure 7.
(A) Structures of DNA-bound AAA+ oligomers reveal different DNA binding approaches used by an evolutionarily related ATPase fold. DnaC (determined here); DnaA PDB ID 3R8F (Duderstadt et al., 2011); IstB PDB ID 5BQ5 (Arias-Palomo and Berger, 2015); ORC-Cdc6 PDB ID 5UDB (Yuan et al., 2017); archaeal initiator Orc1 PDB ID 2QBY (Dueber et al., 2007).
(B) Individual domains of the structures shown in (A) reveal that initiator clade AAA+ proteins use different faces of their shared ISM element (red) to engage DNA.

A

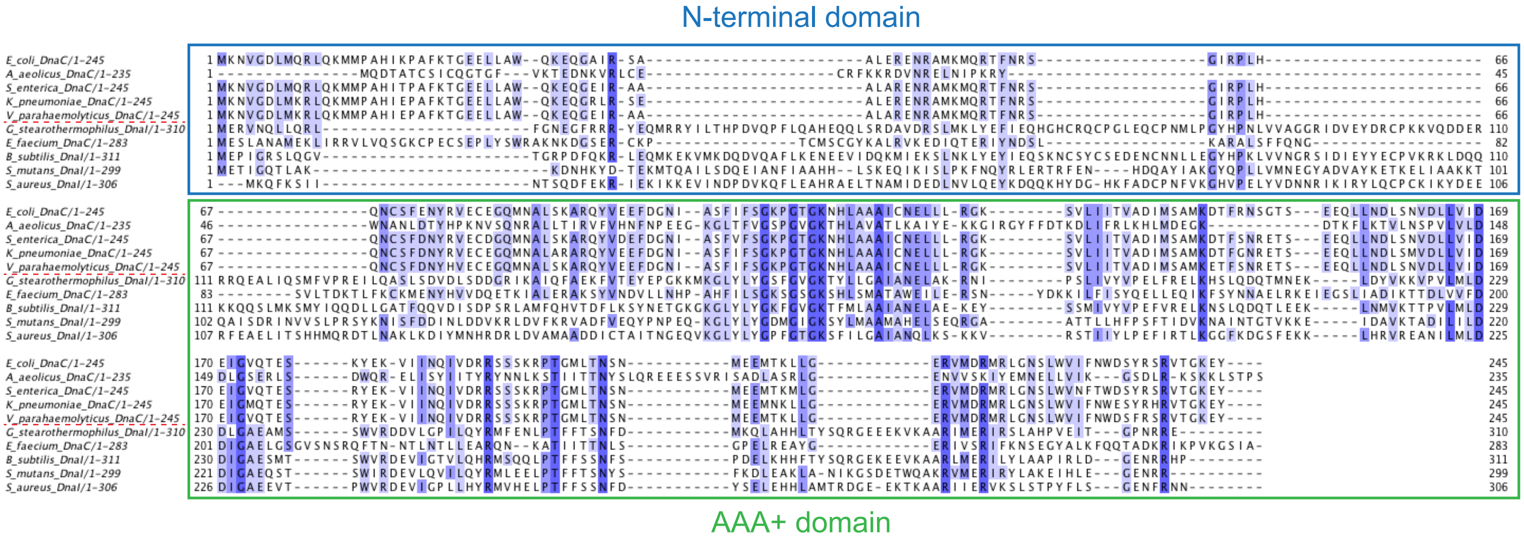

Figure S7. The N-terminal region of bacterial helicase loaders differs substantially between Gram-positive and -negative organisms, related to Figure 7.

(A) Multiple sequence alignment of helicase loaders (DnaC and DnaI). The dotted red line separates Gram-negative (upper sequences) from Gram-positive bacteria (lower sequences). Sequence alignments were generated with MAFFT7.407 and plotted using Jalview2.10.5.